UCLA
UCLA Previously Published Works

Title
Ultrahigh vacuum dc magnetron sputter-deposition of epitaxial Pd(111)/Al2O3(0001) thin films

Permalink
https://escholarship.org/uc/item/6x13278f

Journal
Journal of Vacuum Science & Technology A Vacuum Surfaces and Films, 36(3)

ISSN
0734-2101

Authors
Aleman, Angel
Li, Chao
Zaid, Hicham
et al.

Publication Date
2018-05-01

DOI
10.1116/1.5021609

Peer reviewed

eScholarship.org Powered by the California Digital Library
University of California

Ultrahigh vacuum dc magnetron sputter-deposition of epitaxial $Pd(111)/Al_2O_3(0001)$ thin films

Angel Aleman, Chao Li, and Hicham Zaid
Department of Materials Science and Engineering, University of California Los Angeles, Los Angeles, California 90095

Hanna Kindlund
Department of Solid State Physics, Lund University, Lund 22100, Sweden

Joshua Fankhauser, Sergey V. Prikhodko, Mark S. Goorsky, and Suneel Kodambaka[a)]
Department of Materials Science and Engineering, University of California Los Angeles, Los Angeles, California 90095

(Received 5 January 2018; accepted 7 March 2018; published 23 March 2018)

Pd(111) thin films, ~245 nm thick, are deposited on $Al_2O_3(0001)$ substrates at $\approx 0.5T_m$, where T_m is the Pd melting point, by ultrahigh vacuum dc magnetron sputtering of Pd target in pure Ar discharges. Auger electron spectra and low-energy electron diffraction patterns acquired *in situ* from the as-deposited samples reveal that the surfaces are compositionally pure 111-oriented Pd. Double-axis x-ray diffraction (XRD) ω-2θ scans show only the set of Pd 111 peaks from the film. In triple-axis high-resolution XRD, the full width at half maximum intensity Γ_ω of the Pd 111 ω-rocking curve is 630 arc sec. XRD 111 pole figure obtained from the sample revealed six peaks 60°-apart at a tilt angles corresponding to Pd 111 reflections. XRD ϕ scans show six 60°-rotated 111 peaks of Pd at the same ϕ angles for $11\bar{2}3$ of Al_2O_3 based on which the epitaxial crystallographic relationships between the film and the substrate are determined as $(111)_{Pd}||(0001)_{Al_2O_3}$ with two in-plane orientations of $[11\bar{2}]_{Pd}||[11\bar{2}0]_{Al_2O_3}$ and $[2\bar{1}\bar{1}]_{Pd}||[11\bar{2}0]_{Al_2O_3}$. Using triple axis symmetric and asymmetric reciprocal space maps, interplanar spacings of out-of-plane (111) and in-plane $(11\bar{2})$ are found to be 0.2242 ± 0.0003 and 0.1591 ± 0.0003 nm, respectively. These values are 0.18% lower than 0.2246 nm for (111) and the same, within the measurement uncertainties, as 0.1588 nm for $(11\bar{2})$ calculated from the bulk Pd lattice parameter, suggesting a small out-of-plane compressive strain and an in-plane tensile strain related to the thermal strain upon cooling the sample from the deposition temperature to room temperature. High-resolution cross-sectional transmission electron microscopy coupled with energy dispersive x-ray spectra obtained from the $Pd(111)/Al_2O_3(0001)$ samples indicate that the Pd-Al_2O_3 interfaces are essentially atomically abrupt and dislocation-free. These results demonstrate the growth of epitaxial Pd thin films with (111) out-of-plane orientation with low mosaicity on $Al_2O_3(0001)$. *Published by the AVS.*
https://doi.org/10.1116/1.5021609

I. INTRODUCTION

Palladium is a group 10 transition-metal with face-centered cubic (fcc) crystal structure with bulk lattice parameter $a_{ref} = 0.3890$ nm at room temperature.[1] Within the platinum-group metals, Pd has the lowest density (12.02 g/cm^3), lowest melting point ($T_m = 1827$ K), with a tensile strength of 196.2 MPa, and an elastic modulus of 121 GPa.[2] Palladium is a well-known catalyst used in the automobile catalytic converters to eliminate harmful emissions produced by the engines.[3] Owing to unusually high capacity of Pd for hydrogen absorption (up to 900 times its volume), Pd and its alloys are attractive for hydrogen storage and in fuel cells.[4,5] Pd-based alloy membranes are used in generation and supply of ultrahigh purity hydrogen.[6] While shape- and size-selected nanocrystals are preferred as catalysts,[7] thin films are desirable for applications such as jewelry, sensors (gas and temperature), coatings, dentistry, electronics, etc.[3] Pd is also considered as one of the best metal contacts for graphene and carbon nanotube based devices.[8] More recently, 111-oriented Pd thin films and single-crystals, owing to high carbon solubility (~1.5 at. % at ~900 K),[9] have been used to grow two-dimensional graphene layers.[10–12]

Pd thin films are most commonly grown via evaporation and sputter-deposition. Previous studies have shown that the morphology and crystallinity of Pd evaporated onto Al_2O_3 substrates depend on the quality of the substrate and the deposition conditions.[13–15] Three-dimensional Pd crystallites formed via evaporation onto single-crystalline oxides [$Al_2O_3(11\bar{2}0)$, $Al_2O_3(0001)$, $Al_2O_3(2\bar{1}\bar{1}0)$, $WO_3(111)$, and $WO_3(001)$], preferentially grow along 111, independent of substrate orientation and composition;[16–18] the in-plane orientations of the Pd thin films, however, are determined by the lattice match; on $Al_2O_3(0001)$ and $Al_2O_3(2\bar{1}\bar{1}0)$, crystallite size dependent contraction (expansion) in out-of-plane (in-plane) Pd lattice parameters have been observed.[17] Heteroepitaxial growth of ultrathin (3–50 nm thick) Pd films on MgO(001), MgO(110), $Al_2O_3(11\bar{2}0)$, and $Al_2O_3(0001)$

[a)]Electronic mail: kodambaka@ucla.edu

 0734-2101/2018/36(3)/030602/6/$30.00

substrates has been demonstrated via sputter-deposition. In that study, the out-of-plane lattice parameter of Pd thin films is found to be the same as the bulk value.[19] Optimal glow-discharge sputter-deposition parameters required for cube-on-cube epitaxial growth of Pd on MgO(001) and NaCl(100) have also been identified.[20]

In this letter, we report the growth of high-quality Pd(111)/Al_2O_3(0001) thin films using ultrahigh vacuum (UHV) dc magnetron sputtering at substrate temperatures $T_s = 873$ and 923 K in an Ar atmosphere. Using a combination of *in situ* Auger electron spectroscopy (AES) and low-energy electron diffraction (LEED) and *ex situ* double-axis x-ray diffraction (XRD) and triple-axis high-resolution XRD (HRXRD), cross-sectional transmission electron microscopy (XTEM), energy dispersive x-ray spectroscopy (EDS), and high-resolution TEM (HRTEM), we determine the surface as well as bulk composition and crystallinity. Our results indicate that the as-deposited Pd layers are: compositionally-pure with ordered surfaces and abrupt Pd-Al_2O_3 interfaces; oriented bi-crystals with two in-plane orientations 60° relative to each other, whose out-of-plane and in-plane orientations with respect to the substrate are Pd(111)||Al_2O_3(0001), and Pd[$\bar{1}\bar{1}2$]||Al_2O_3[$11\bar{2}0$] and Pd [$2\bar{1}\bar{1}$]||Al_2O_3[$11\bar{2}0$], respectively.

II. EXPERIMENTAL PROCEDURE

A. Thin film deposition

The Pd films are grown using a procedure similar to that used for the growth of Zr/Al_2O_3(0001) thin films in a custom-designed dual-chamber UHV deposition system (base pressure $\sim 2.0 \times 10^{-10}$ Torr) equipped with a dc magnetron (Kurt J. Lesker), LEED/AES assembly (LK Technologies), and a residual gas analyzer (Pfeifer Vacuum).[21] The substrates are single-side polished 0.5-mm-thick, $2 \times 10\,mm^2$ rectangular strips of Al_2O_3(0001) cut from $10 \times 10\,mm^2$ single-crystals (MTI). The Al_2O_3(0001) strips are cleaned by sonication sequentially in acetone, isopropanol, and deionized water. The substrates are then dried by heating in air for 1 h at 523 K after which they are mounted on a pyrolytic boron nitride heater, and transferred into the deposition chamber. The sample is degassed at 1273 K until the chamber pressure is below 6.0×10^{-9} Torr, after which the T_s is set to the desired temperature (873 and 923 K). All the temperature values reported here are measured at the center of bare Al_2O_3 substrate placed on Mo heater foil using Mo emissivity[21] of 0.13 and do not account for plasma heating during sputter-deposition. The maximum variation in T_s across the substrate is ±100 K. For details, please see Ref. 21.

The magnetron is equipped with a 50-mm-diameter × 3-mm-thick Pd (99.99% pure from ACI Alloys, Inc.) target. Pd films are grown using a constant target power of 50 W (320 V) in 20 mTorr Ar (99.999% pure) discharge with the Ar introduced through an UHV leak valve. (Prior to deposition, the target is sputter-cleaned using the same deposition parameters for 3 min with the sample rotated out-of-sight from the target.) The deposition time is 15 min. This procedure yields Pd films with a nominal thickness of 266 ± 3 nm, as measured from cross-sectional TEM images. Based upon this data, we estimate a deposition rate of ~0.3 nm/s. After deposition, the Ar gas supply is shut off and the chamber is evacuated while the sample is passively cooled to room temperature by switching off the current supplied to the substrate heater.

B. Characterization

The as-deposited Pd sample surface composition and structure are determined *in situ* using UHV-compatible, reverse-view, LEED/AES system with four-grid optics.[21] The Auger electron spectra are acquired in derivative mode using a 1 keV primary beam and a beam current of up to 50 μA at kinetic energies between 130 and 550 eV with a step size of 0.165 eV and a dwell time of 0.2 s. LEED patterns are obtained at incident electron energies between 60 and 250 eV using a screen voltage of 4 kV and a Can aperture voltage of 14 V.

All the following XRD measurements—symmetric ω-2θ spectra, ω-rocking curves, the pole figure, high-resolution symmetric and asymmetric reciprocal space maps (RSMs), and ϕ scans, where ϕ is the in-plane angular rotation around the surface normal relative to a certain reference position—are performed using a Jordan Valley D1 diffractometer. The incident monochromatic Cu Kα_1 beam is generated with a sealed source, a Göbel specular mirror, and a Si(220) two reflection collimator crystal.[21] The ω-2θ scan over a large range of 30°–100°, the pole figure, and ϕ scans are performed under double-axis diffraction condition, the ω-2θ scans and ω-rocking curves around Pd 111 and Pd 222 reflections, and the symmetric and asymmetric RSM are conducted under triple-axis diffraction condition. The diffracted beam is conditioned in double-axis diffraction using slits with ~0.36° acceptance angle for the ω-2θ scan, and Soller slits for the pole figures and ϕ scans. A Si(220) two reflection analyzer crystal with an acceptance angle of ~0.003° is used for the triple-axis diffraction condition in the HRXRD measurements. We use $2\theta = 41.68°$, corresponding to the 0006 reflection of Al_2O_3 single-crystal with $c_s = 1.2991$ nm,[22] for calibration of the sample and the stage with respect to ω and χ (out-of-plane rotation perpendicular to ω), and $11\bar{2}9$ reflection of Al_2O_3 single-crystal for calibration of the sample and stage with respect to ϕ. ω-2θ data using double-axis diffraction are obtained over a range of 2θ values between 30° and 100° in steps of 0.02° with a dwell time of 1 s. Pole figure data are obtained from the Pd/Al_2O_3(0001) sample while scanning ϕ from 0° to 360° in steps of 1° at each χ between −80° and +80°, varied in steps of 2°. The ϕ scans of skew-symmetric Pd 111 and Al_2O_3 $11\bar{2}3$ reflections are collected with a step size of 0.05° and a dwell time of 0.5 s in the parallel-beam mode with $\chi = 70.5°$ for Pd and $\chi = 61.2°$ for Al_2O_3. For both pole figure and ϕ-scan measurements, 2θ and ω angles are fixed at 40.14° and 20.07°, respectively, to detect Pd 111 reflections. For the ϕ-scan of the Al_2O_3 substrate, 2θ is fixed at 43.397° and ω at 21.699° to detect Al_2O_3 $11\bar{2}3$ reflections. High resolution symmetric ω-2θ spectra of Pd 111 and 222 reflections are measured over ranges of 0.9° and 2.3° with step sizes of 4 and 10 arc sec, respectively. High resolution ω-

rocking curves of Pd 111 and 222 reflections are measured over ranges of 0.7° and 0.5° with step sizes of 40 and 90 arc sec, respectively. The dwell times for both high resolution symmetric ω-2θ spectrum and ω-rocking curve of Pd 111 are 0.5 s, and those for the same measurements of Pd 222 is 1 s. High-resolution symmetric Pd 222 and Al_2O_3 00012 (asymmetric Pd 113 and Al_2O_3 $11\bar{2}9$) RSMs are acquired over a range of 2.3° (2.8°) in ω-2θ with a step size of 10 (60) arc sec and 0.5° (2.4°) in ω with a step size of 90 (200) arc sec and dwell time of 1 s (0.1 s).

The Pd/Al_2O_3(0001) XTEM samples are prepared via milling using 30 kV Ga^+ ions in an FEI Nova 600 NanoLab DualBeam™ scanning electron microscope/focused ion beam (FIB) system. Prior to FIB milling, the film surface is protected by sequential deposition of thin (~50 nm) and thick (~150 nm) layers of Pt using 30 kV, 0.1 nA electron and ion beams, respectively. The XTEM samples are first examined in a JEOL 100CX TEM operated at 100 kV. High resolution TEM images, selected area electron diffraction (SAED) patterns, and EDS measurements are all acquired in an FEI Titan 80–300 kV scanning TEM operated at 300 kV.

III. RESULTS AND DISCUSSION

Figures 1(a) and 1(b) are typical *in situ* AES and LEED data, respectively, obtained from sputter-deposited Pd/Al_2O_3(0001) samples. The Auger electron spectrum [Fig. 1(a)] reveals one peak with the highest intensity at 330 eV and several lower intensity peaks at 190, 243, and 279 eV, all of which we attribute to Pd.[23,24] We do not observe any peaks associated with common contaminants such as C (272 eV), N (382 eV), and O (503 eV). The LEED pattern [Fig. 1(b)] shows sixfold symmetric set of spots, suggestive of (1 × 1) structure of unreconstructed fcc(111) surface. Both these results are a first indication that the as-deposited Pd layers are compositionally pure with highly ordered surfaces.

Pd layer crystalline quality is determined using double-axis XRD and triple-axis HRXRD. Over the entire range of 2θ values between 30° and 100° in the double-axis ω-2θ measurement, we observe only two sets of peaks, at 40.14° and 86.74° of Pd 111 and Pd 222 peaks, and 41.68° and 90.76° of Al_2O_3 0006 and Al_2O_3 00012 peaks. Figures 2(a) and 2(b) are the HRXRD ω-2θ scans and ω-rocking curves of Pd 111 and Al_2O_3 0006 peaks, respectively. ω-rocking curves for the Pd 111 and the Al_2O_3 0006 diffraction peaks in Fig. 2(b) are aligned such that their peak positions coincide with the origin on the horizontal axis of the plot. For the Pd film, the full width at half maximum intensity (FWHM) Γ_ω of the ω-rocking curve is 630 arc sec, which indicates that only very small out-of-plane misorientations are present in the Pd layer. (The corresponding Γ_{ω,Al_2O_3} for the Al_2O_3 0006 diffraction peak is 15 arc sec.) Using a Williamson–Hall approach[25] with the FWHM of Pd 111 and Pd 222 triple axis ω-2θ scans and ω-rocking curves, we estimate an out-of-plane coherence length of 245 nm and an in-plane coherence length ≥210 nm. There are, of course, rather large error bars associated with a two-point measurement so these values are introduced simply to confirm that the out-of-plane coherence length is comparable to the layer thickness and the in-plane coherence length is of this same dimension or greater. These measurements are also supported by the low-magnification TEM data (not shown), which reveal only a single grain across 1 μm field of view and Pd 113 reflection in the high-resolution asymmetric RSM [Fig. 3(b)], which shows that the mosaic broadening dominates the symmetric reflection peak widths. Thus, only a small contribution to the broadening results from the in-plane coherence length.

Figures 2(c) and 2(d) are XRD pole figure and ϕ scans from the Pd/Al_2O_3(0001) sample. The polar plot in Fig. 2(c) reveals six peaks at $\chi = 70.5°$ and at ϕ values 60° apart, all of which correspond to Pd 111. The absence of peaks at all other χ values implies a strong $\bar{1}\bar{1}2$ in-plane texture in the layer. If all the 111 crystallites within the layer are oriented with the same in-plane orientation, then the pole figure would contain only three peaks at $\chi = 70.5°$ at ϕ values 120° apart. The fact that we observe six 60°-apart peaks indicates that there are two distinct in-plane orientations, i.e., two 111-oriented domains rotated 60° with respect to each other. The plot in Fig. 2(d) shows six 60°-rotated Pd 111 and Al_2O_3 $11\bar{2}3$ diffraction peaks at the same ϕ angles, indicating that the film and the substrate exhibit the same sixfold symmetry. The combination of the XRD ω-2θ, HRXRD ω-rocking curves, pole figure, and ϕ scans demonstrate that our Pd(111) layers grow as 111 oriented bicrystals with in-plane orientational relationships of $[11\bar{2}]_{Pd}||[11\bar{2}0]_{Al_2O_3}$ and $[2\bar{1}\bar{1}]_{Pd}||[11\bar{2}0]_{Al_2O_3}$.

In order to determine the extent of elastic strain, if any, in the Pd layers, we carried out RSM measurements of the Pd/Al_2O_3(0001) layers. Figures 3(a) and 3(b) are high-resolution RSMs acquired around symmetric Pd 222 and asymmetric Pd 113 reflections, respectively. Symmetric RSM of substrate Al_2O_3 around 00012 reflection and asymmetric RSM around $11\bar{2}9$ reflections are used as references in Fig. 3. The plots show isointensity contours of diffracted beam intensities as a function of in-plane $\Delta Q_\parallel$ and out-of-plane $\Delta Q_\perp$ reciprocal space vectors, with symmetric 00012 and asymmetric $11\bar{2}9$ reflections of the Al_2O_3 substrate as the origins. That is, in Fig. 3(a), $\Delta Q_\parallel = Q_\parallel - Q_{\parallel,00012}$ and

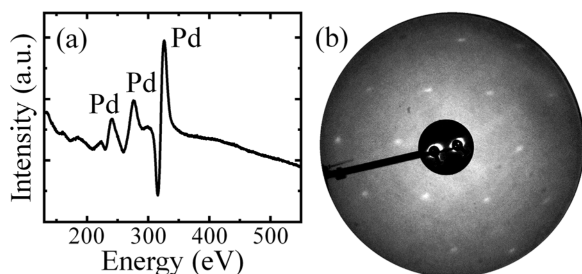

FIG. 1. Representative (a) Auger electron spectrum (AES) acquired *in situ* from ~266-nm-thick Pd/Al_2O_3(0001) thin film after sputter-deposition at $T_s = 923$ K. All the observed peaks at 190, 243, 279, and 330 eV correspond to Pd. We note the absence of peaks associated with C (~272 eV), N (~382 eV), and O (~503 eV). (b) *In situ* LEED pattern obtained from ~5-nm-thick Pd/Al_2O_3(0001) sample grown at $T_s = 873$ K. The incident electron energy is 95 eV. The observed sixfold symmetric set of spots is consistent with the expected face centered cubic (fcc) 111-(1 × 1) surface structure.

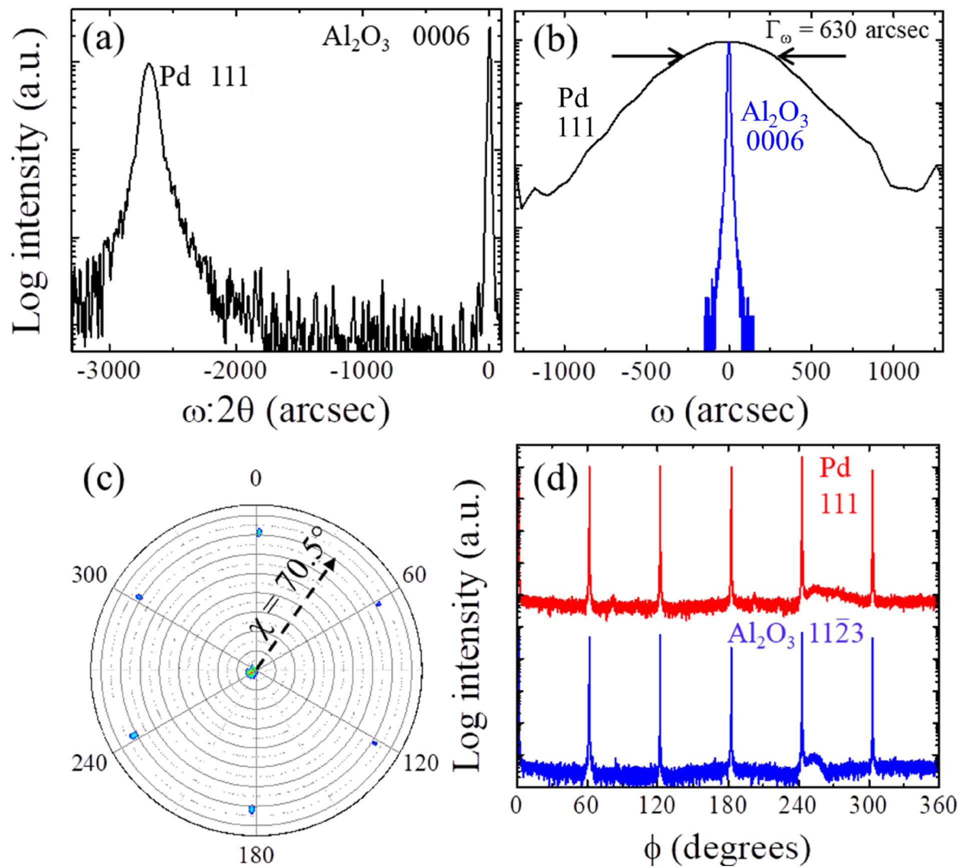

Fig. 2. (Color online) High-resolution x-ray diffraction (HRXRD) (a) ω-2θ scan and (b) Pd 111 and Al_2O_3 0006 ω-rocking curves obtained from the Pd/Al_2O_3(0001) thin film. In both (a) and (b), intensities are plotted on log scales. (c) Pd 111 XRD pole figure obtained with $2\theta = 40.14°$ and (d) Pd 111 (red) and Al_2O_3 11 $\bar{2}$ 3 (blue) XRD ϕ-scans from the same sample.

$\Delta Q_\perp = Q_\perp - Q_{\perp,00012}$; in Fig. 3(b), $\Delta Q_\| = Q_\| - Q_{\|,11\bar{2}9}$ and $\Delta Q_\perp = Q_\perp - Q_{\perp,11\bar{2}9}$, where $Q_\|$ and $Q_\perp$ are related to peak positions in ω-2θ space through the relationships: $Q_\| = (2/\lambda)\sin(\theta)\sin(\theta - \omega)$ and $Q_\perp = (2/\lambda)\sin(\theta)\cos(\theta - \omega)$.

The symmetric RSM shows that Pd 222 and corundum (hexagonal) 00012 reflections are aligned along the $Q_\perp$ axis, indicating the (111) out-of-plane orientation of the Pd layer matches the (0001) corundum substrate orientation. For asymmetric Pd 113 [Al_2O_3 11$\bar{2}$9] reflections, the in-plane and out-of-plane reciprocal space vectors are Pd $\frac{2}{3}(\bar{1}\bar{1}2)$ [Al_2O_3 11$\bar{2}$0] and Pd $\frac{5}{3}$(111) [Al_2O_3 0009], respectively. Using $1/d_{11\bar{2}0} = 2/a_s$,[21] where $a_s = 0.4759$ nm for hexagonal Al_2O_3,[22] $\Delta Q_{\|,113} = [1/d_{11\bar{2}0} - Q_{\|,113}] = 0.014 \pm 0.0084\ \mathrm{nm}^{-1}$ from Fig. 3(b), and since $Q_{\|,113} \equiv \frac{2}{3} Q_{\bar{1}\bar{1}2}$, we obtain $d_{\bar{1}\bar{1}2} = 0.1591$

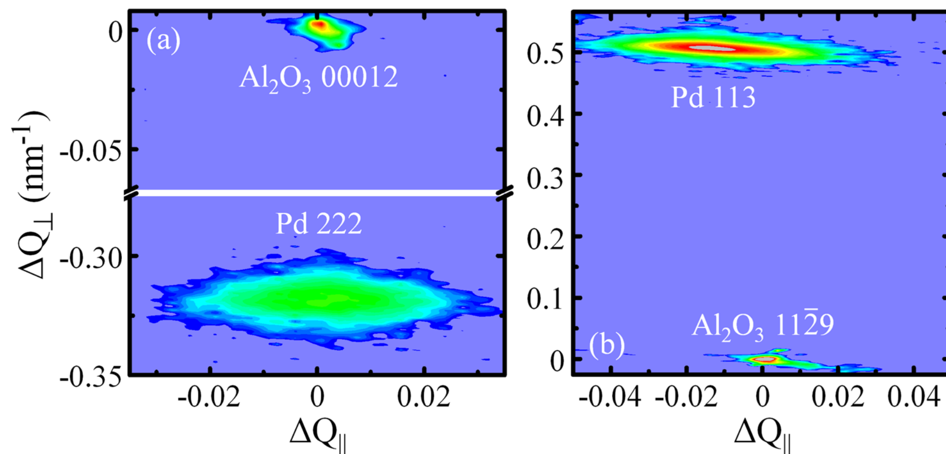

Fig. 3. (Color online) Characteristic high-resolution (a) symmetric and (b) asymmetric RSMs acquired around the symmetric Pd 222 [Al_2O_3 00012] and asymmetric 113 [Al_2O_3 11$\bar{2}$9] reflections, respectively, from the same Pd/Al_2O_3(0001) sample as in Fig. 2. The plots show isointensity diffraction contours as a function of in-plane $\Delta Q_\|$ and out-of-plane $\Delta Q_\perp$ reciprocal lattice vectors measured with respect to the Al_2O_3 00012 [in (a)] and 11$\bar{2}$9 [in (b)] reciprocal lattice vectors as reference.

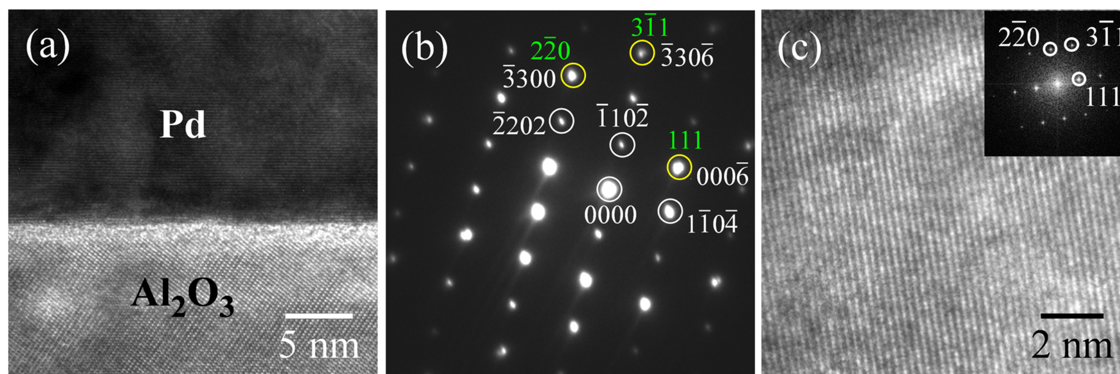

FIG. 4. (Color online) (a) Typical bright-field XTEM image from a Pd(111)/Al_2O_3(0001) sample showing the region around Pd-Al_2O_3 interface. (b) SAED pattern obtained from the Pd-Al_2O_3 interface region shown in (a) with Pd $[11\bar{2}]$ and Al_2O_3 $[\bar{1}\bar{1}20]$ as zone axes. Substrate and film reflections are indexed using Bravais-Miller and Miller indices, respectively, as shown. (c) Higher resolution XTEM image of the Pd film shown in (a). Inset is a Fourier transform of the image showing sixfold symmetric spots indexed as shown.

$\pm$ 0.0003 nm. Following a similar approach, with $\Delta Q_{\perp,113} = [Q_{\perp,113} - 1/d_{0009}] = 0.507 \pm 0.0097\ \text{nm}^{-1}$ from Fig. 3(b) and $Q_{\perp,113} \equiv \frac{5}{3} Q_{111}$, we determine $d_{111} = 0.2242 \pm 0.0003$ nm. Compared with $d_{\bar{1}\bar{1}2} = 0.1588$ nm and $d_{111} = 0.2246$ nm, calculated from the lattice parameter a_{ref} of bulk Pd, the measured d spacing along the in-plane direction is, within the measurement uncertainties, the same while that along the out-of-plane direction is 0.18% lower. These results are indicative of a small out-of-plane compressive strain and in-plane tensile strain in the lattice. This is partly due to differential thermal contraction of the substrate and the film [coefficient of thermal expansion of Pd (Ref. 26) is 11.8×10^{-6}/K and that of Al_2O_3 is 5.2×10^{-6}/K along the basal plane,[22] which would lead to an in-plane tensile thermal strain of 0.41% in the Pd layer] upon cooling the sample from T_s to room-temperature.

Figure 4(a) is a typical bright-field XTEM image acquired from near the interface region of the Pd(111)/Al_2O_3(0001) sample. From this and other XTEM images along with EDS data (not shown), we find that the Pd-Al_2O_3 interface is atomically abrupt. Moreover, we do not find any evidence of the presence of misfit dislocations at the interface. Figure 4(b) is a SAED pattern from the Pd-Al_2O_3 interface along the Pd $[11\bar{2}]$ zone-axis. A few of the Pd reflections (e.g., 111, $2\bar{2}0$, and $3\bar{1}1$) appear superposed, due to similar interplanar spacings, with those of the Al_2O_3 substrate. The spot pattern confirms that the Pd film is single-crystalline. Lattice-resolved XTEM image of the Pd layer along with a Fourier transform of the image are shown in Fig. 4(c). Interplanar spacings measured from the single-crystalline 111 reflections in the SAED pattern and in the Fourier transform are $\approx$0.230 and $\approx$0.229 nm, respectively. These values are, within measurement uncertainties of $\pm$0.007 nm, comparable with the RSM data.

IV. CONCLUSIONS

In summary, we demonstrate the growth of Pd thin films with nearly fully relaxed, 111 oriented bi-crystals on Al_2O_3(0001) via ultrahigh vacuum dc magnetron sputter-deposition at temperatures approximately half the homologous melting point of Pd. Using *in situ* surface characterization techniques, Auger electron spectroscopy and low-energy electron diffraction, we show that the as-deposited Pd layers are free of common contaminants such as carbon, nitrogen, and oxygen and with (1×1)-Pd(111) structure. Using a combination of double-axis x-ray diffraction ω-2θ, pole figure, ϕ scans, and triple-axis HRXRD ω-rocking, we determine that the Pd thin films are face centered cubic that are oriented with respect to the substrate as $(111)_{\text{Pd}}||(0001)_{Al_2O_3}$ with $[11\bar{2}]_{\text{Pd}}||[11\bar{2}0]_{Al_2O_3}$ and $[2\bar{1}\bar{1}]_{\text{Pd}}||[11\bar{2}0]_{Al_2O_3}$. The in-plane and out-of-plane lattice parameters extracted from high-resolution symmetric and asymmetric reciprocal space maps reveal that the Pd layers are in a state of low residual in-plane tensile strain that arises, most likely, from the differences in thermal contraction of the substrate and the film upon cooling from the growth temperature to room-temperature. Transmission electron microscopy, electron diffraction, and energy dispersive x-ray spectroscopic characterization of the Pd(111)-Al_2O_3(0001) interfaces show that the interfaces are atomically abrupt and free of any structural defects. We expect that our results will be of interest to catalysis, hydrogen sensor, and nanoelectronic applications, where high-quality thin films are desirable.

ACKNOWLEDGMENTS

The authors gratefully acknowledge support from the Air Force Office of Scientific Research (AFOSR, Ali Sayir) under Grant No. FA9550-14-1-0106 and the Office of Naval Research Grant No. N00014-12-1-0518 (Chagaan Baatar) for the funds used to build the UHV deposition system. A.A. is supported by the National Science Foundation Grant No. 1563427 (Kara Peters). The authors thank Noah Bodzin and the Nanoelectronics Research Facility in the UCLA Henry Samueli School of Engineering for assistance with FIB milling and acknowledge the use of instruments at the Electron Imaging Center for NanoMachines supported by NIH (1S10RR23057) and the California NanoSystems Institute at UCLA.

[1]A. Kern and W. Eysel, *Mineralogisch-Petrograph* (Inst., Univ. Heidelberg, Germanny, ICDD Grant-in-Aid, 1993).
[2]F. Habashi, *Handbook of Extractive Metallurgy* (Wiley-VCH, Federal Republic of Germany, 1997).

[3]H. Renner *et al.*, *Ullmann's Encyclopedia of Industrial Chemistry* (Wiley, 2001).
[4]T. B. Flanagan and W. A. Oates, Annu. Rev. Mater. Sci. **21**, 269 (1991).
[5]F. Favier, E. C. Walter, M. P. Zach, T. Benter, and R. M. Penner, Science **293**, 2227 (2001).
[6]S. N. Paglieri and J. D. Way, Sep. Purif. Methods **31**, 1 (2002).
[7]G. J. Leong *et al.*, Nanoscale **6**, 11364 (2014).
[8]F. Xia, V. Perebeinos, Y.-M. Lin, Y. Wu, and P. Avouris, Nat. Nanotechnol. **6**, 179 (2011).
[9]T. B. Massalski, H. Okamoto, P. Subramanian, and L. Kacprzak, *Binary Alloy Phase Diagrams* (ASM International, OH, 1990).
[10]H. S. Mok, A. Ebnonnasir, Y. Murata, S. Nie, K. F. McCarty, C. V. Ciobanu, and S. Kodambaka, Appl. Phys. Lett. **104**, 101606 (2014).
[11]Y. Murata, S. Nie, A. Ebnonnasir, E. Starodub, B. B. Kappes, K. F. McCarty, C. V. Ciobanu, and S. Kodambaka, Phys. Rev. B **85**, 205443 (2012).
[12]S. Y. Kwon, C. V. Ciobanu, V. Petrova, V. B. Shenoy, J. Bareno, V. Gambin, I. Petrov, and S. Kodambaka, Nano Lett. **9**, 3985 (2009).
[13]H. Poppa, E. H. Lee, and R. D. Moorhead, J. Vac. Sci. Technol. **15**, 1100 (1978).
[14]M. Bäumer, J. Libuda, A. Sandell, H. J. Freund, G. Graw, T. Bertrams, and H. Neddermeyer, Ber. Bunsen-Ges. Phys. Chem. **99**, 1381 (1995).
[15]V. Jayaraman, Y. S. Lin, M. Pakala, and R. Y. Lin, J. Membr. Sci. **99**, 89 (1995).
[16]K. Mašek and V. Matolín, Vacuum **50**, 151 (1998).
[17]K. Mašek and V. Matolín, Eur. Phys. J. D **9**, 557 (1999).
[18]K. Mašek, S. Nemšák, and V. Matolín, Vacuum **82**, 274 (2007).
[19]G. R. Harp and S. S. P. Parkin, Thin Solid Films **288**, 315 (1996).
[20]F. Reniers, M. P. Delplancke, A. Asskali, V. Rooryck, and O. Van Sinay, Appl. Surf. Sci. **92**, 35 (1996).
[21]J. Fankhauser, M. Sato, D. Yu, A. Ebnonnasir, M. Kobashi, M. S. Goorsky, and S. Kodambaka, J. Vac. Sci. Technol., A **34**, 050606 (2016).
[22]E. R. Dobrovinskaya, L. A. Lytvynov, and V. Pishchik, *Sapphire: Material, Manufacturing, Applications* (Springer, Boston, MA, 2009), pp. 55–176.
[23]G. Maire, L. Hilaire, P. Legare, F. G. Gault, and A. O'Cinneide, J. Catal. **44**, 293 (1976).
[24]L. E. Davis, N. C. MacDonald, P. W. Palmberg, G. E. Riach, and R. E. Weber, *Handbook of Auger Electron Spectroscopy* (Physical Electronics Industries, Eden Prairie, MN, 1976), Vol. 27, No. 6.
[25]H.-M. Wang, J.-P. Zhang, C.-Q. Chen, Q. Fareed, J.-W. Yang, and M. A. Khan, Appl. Phys. Lett. **81**, 604 (2002).
[26]D. R. Lide, *CRC Handbook of Chemistry and Physics* (CRC, Boca Raton, FL, 2012).